Original Paper

Comparative study of the adsorption of tetracycline on clay minerals with various nanostructures: allophane, halloysite, and montmorillonite

Qiyi Ma[1,2], Ning Zhao[1,2], Shun Wang[3,4] , Baifa Zhang[1], Mengyuan Li[2] , Dong Liu[2] , Xiang Zhou[5], Maxim Rudmin[6] , Antoine F. Mulaba-Bafubiandi[7] and Peng Yuan[1]

[1]School of Environmental Science and Engineering, Guangdong University of Technology, Guangzhou, 510006, China; [2]CAS Key Laboratory of Mineralogy and Metallogeny/Guangdong Provincial Key Laboratory of Mineral Physics and Materials, Guangzhou Institute of Geochemistry, Chinese Academy of Sciences, Guangzhou, 510640, China; [3]Key Laboratory of Comprehensive and Highly Efficient Utilization of Salt Lake Resources/Qinghai Provincial Key Laboratory of Geology and Environment of Salt Lakes, Qinghai Institute of Salt Lakes, Chinese Academy of Sciences, Xining, 810008, China; [4]Songshan Lake Materials Laboratory, Dongguan, 523808, China; [5]Jewelry Institute, Guangzhou Panyu Polytechnic, Guangzhou, 511483, China; [6]Tomsk Polytechnic University, 634050 Tomsk, Russia and [7]Mineral Processing and Technology Research Centre, Department of Metallurgy, School of Mining, Metallurgy and Chemical Engineering, Faculty of Engineering and the Built Environment, University of Johannesburg, PBOX 17011 South Africa

Abstract

With the over-use of tetracycline (TC) and its ultimate accumulation in aquatic systems, the demand for TC removal from contaminated water is increasing due to its severe threat to public health. Clay minerals have attracted great attention as low-cost adsorbents for controlling water pollution. The objective of the present study was to measure the adsorption behavior and mechanisms of TC on allophane, a nanosized clay mineral with a hollow spherical structure; to highlight the advantage of the allophane nanostructure, a further objective was to compare allophane with halloysite and montmorillonite, which have nanostructures that differ from allophane. Structural features and surface physicochemical properties were characterized by transmission electron microscopy (TEM), Fourier-transform infrared spectroscopy (FTIR), X-ray diffraction (XRD), zeta potential, N_2-physisorption, and acid–base titration. The adsorption data showed that TC adsorption followed the pseudo-second order and Langmuir models. The adsorption was pH dependent, as all three clay minerals performed better under neutral to weakly alkaline conditions and maintained high adsorption performance in the presence of co-existing $Na^+/K^+/Ca^{2+}/Mg^{2+}$ cations. Regeneration of the adsorbent was excellent, with efficiencies exceeding 75% after five recycles. By comparison, allophane always exhibited the greatest adsorption capacity, up to 796 mg g^{-1} at ~pH 9. The TC adsorption on allophane and halloysite was dominated by inner-sphere complexation, together with a small amount of electrostatic adsorption, while that on montmorillonite involved mainly interlayer cation exchange. The findings provide insights into the effects of nanostructures of clay minerals on their TC adsorption performance and highlight the huge potential of allophane as an efficient and inexpensive adsorbent for TC removal.

Keywords: allophane; clay mineral; interfacial interactions; tetracycline adsorption

Introduction

Tetracycline (TC), an effective and inexpensive broad-spectrum antibiotic, has been widely used for human beings and animals to prevent or treat bacteria-caused infections. TC was reported to be the second most used antibiotic worldwide in the year 2020 (Leichtweis et al., 2022). However, the majority (70–95%) of TC in animals is excreted into the environment (Qiao et al., 2020). TC and its derivatives are environmentally persistent and readily accumulate in aquatic environments, thereby negatively affecting the ecosystem and human health (Xiao et al., 2021; Xu et al., 2021). Therefore, the demand is increasing for efficient, economical, and eco-friendly removal of TC from contaminated waters.

Various technologies have been developed for TC removal, such as adsorption, membrane filtration, and chemical/photochemical degradation (Gopal et al., 2020; Leichtweis et al., 2022). The adsorption method is most widely accepted due to its advantages of easy operation, low consumption, and re-usability. Many adsorbents have been designed, of which nanomaterials usually exhibit excellent performance due to their surface activity and large specific surface area arising from their unique nanostructures (Xiong et al., 2018; Zhang et al., 2018; Qiao et al., 2020; Wang et al., 2021). However, the manufacture of nanomaterials often consumes

abundant chemical reagents and produces secondary pollution, thus limiting their practical applications.

As a kind of natural nanomaterial, clay minerals have been widely considered to be sustainable adsorbents for water-pollution control (Peng et al., 2015; Feng et al., 2019; Yang et al., 2021; Ewis et al., 2022). Some studies have conducted the TC adsorption on various clay minerals, such as illite (Chang et al., 2012), kaolinite (Bansal, 2013), halloysite (Zhang et al., 2021), and montmorillonite (Parolo et al., 2008; Wu et al., 2019; Maged et al., 2020). Allophane (1–2SiO$_2$·Al$_2$O$_3$·5–6H$_2$O) is a natural nanosized clay mineral and commonly shows some physicochemical properties similar to nanomaterials due to its unique hollow spherical structure. Allophane consists of 3.5–5.0 nm diameter hollow spherules, of which the spherule wall that contains several defect pores (0.35–0.5 nm) is composed of a curved gibbsite-like sheet with orthosilicate/oligomeric silicate groups attached to its inside. As a result, allophane has plenty of surface hydroxyl groups and a large specific surface area (200–500 m^{2}g^{-1}, theoretically up to >1000 m^{2}g^{-1}) (Huang et al., 2016; Wang et al., 2020), thereby exhibiting large adsorption capacities to polar organic matter (e.g. DNA, fatty acids, norfloxacin, ciprofloxacin) (Nishikiori et al., 2010; Huang et al., 2016; Ma et al., 2023a; Ma et al., 2023b). Accordingly, allophane presumably should show a strong affinity towards TC, but the actual adsorption of TC to it is not fully understood.

The goal of the present study, therefore, was to evaluate the performance of, and mechanisms for, the adsorption of TC to hollow, spherical allophane, and to highlight the nanostructural advantage of allophane over two other clay minerals with different nanostructures, namely 1:1 layered nanotubular halloysite and 2:1 layered montmorillonite. Results from this study are expected to expand the application of allophane in the control of environmental pollution and to provide fundamental knowledge for the development of efficient and environmentally friendly TC adsorbent materials based on clay minerals.
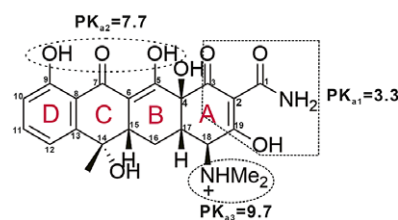
Materials and methods

Materials and chemicals

To avoid the interference of impurities, allophane was obtained via a synthetic method as reported previously (Wang et al., 2020). Because the drying process might cause serious and irreversible aggregation of allophane nanoparticles (Du et al., 2020), an allophane suspension (mass concentration of ~5 mg mL^{-1}) without drying was used for adsorption. Halloysite and montmorillonite powders with high purity were sourced from mine deposits in Shanxi Province and Inner Mongolia, China, respectively; both clay minerals were purified by a conventional sedimentation method and then passed through a 200 mesh sieve. The chemical composition of the clay minerals (Table 1) was determined by an X-ray fluorescence spectrometer (XRF) (Shimadzu XRF-1800). The cation exchange

Figure 1. Planar chemical structure of the tetracycline molecule and its pK$_a$ values (Kulshrestha et al., 2004).

capacities (CEC) of allophane, halloysite, and montmorillonite were 85, 31, and 108 mmol g^{-1}, respectively, determined by the hexaamminecobalt trichloride method (Zhu et al., 2007).

Tetracycline, NaCl, KCl, CaCl$_2$, MgCl$_2$, NaOH, Na$_2$CO$_3$, HCl, and potassium hydrogen phthalate of AR grade were purchased from Shanghai Maclin Biochemical Technology Co., Ltd, China. Solutions were prepared using deionized water (18.25 MΩ cm). TC is known to show three pK$_a$ values (3.3, 7.7, 9.7) due to its tricarbonyl amide (C-1; C-2; C-3), phenol diketone (C-5; C-7; C-9), and dimethylamine (C-18) groups (Fig. 1). It appears mainly in cationic form at pH ≤3.3, zwitterionic form at pH 3.3–7.7, and anionic form at pH >7.7 (Kulshrestha et al., 2004).

Adsorption experiments

The adsorption behavior of TC on the clay minerals was investigated through batch adsorption experiments. Five milligrams of the clay mineral was mixed with 50 mL of TC solution (100 mg L^{-1}) in a 100 mL Erlenmeyer flask followed by shaking on a thermostatic shaker at a speed of 200 rpm at 25°C. The suspension pH was kept at 7 (adjusting with 0.1 M HCl or NaOH solution, <0.1 mL per addition). After adsorption, suspensions were centrifuged at 10,000×g for 10 min, and the supernatants were collected to measure the TC concentration using a PC TU-1810 UV-Vis spectrophotometer at 275 nm. The adsorption capacity (q_e, mg g^{-1}) was calculated as follows:

$$q_e = \frac{(C_0 - C_e) \times V}{m}, \qquad (1)$$

where C_0 and C_e (mg L^{-1}) are the TC concentrations before and after adsorption, respectively; V (mL) is the volume of TC solution, and m (g) is the mass of adsorbent.

Measurements were taken at various time intervals ranging from 1 to 1440 min and the resulting kinetic data were fitted to the pseudo-first order (Eqn 2) and pseudo-second order (Eqn 3) models:

$$\ln(q_e - q_t) = \ln q_e - k_1 t \qquad (2)$$

$$q_t = \frac{k_2 q_e^2 t}{1 + k_2 q_e^2 t} \qquad (3)$$

where q_e and q_t (mg g^{-1}) represent the adsorption capacities at equilibrium and adsorption time t (min); and k$_1$ (min^{-1}) and k$_2$ (g mg^{-1} min^{-1}) are the kinetic constants for the above-mentioned kinetic models, respectively.

For adsorption isotherms, the C_0 of TC solution was set in the range of 10–100 mg L^{-1} with an interval of 10 mg L^{-1}. The pH of the suspension was kept at ~7. After adsorption for 720 min, the C_e of TC in supernatants was measured and the adsorption capacities (q_e)

Table 1. Chemical composition of three clay minerals determined by XRF (wt.%)

Clay mineral	SiO$_2$	Al$_2$O$_3$	Na$_2$O	K$_2$O	MgO	CaO	Fe$_2$O$_3$	Others
Allophane	61.38	37.77	—	—	—	—	—	0.85
Halloysite	49.82	48.85	—	0.10	—	0.15	0.07	1.01
Montmorillonite	62.18	23.28	5.14	0.50	4.67	2.29	1.65	0.29

were calculated. Isothermal adsorption data were described by the Langmuir (Eqn 4) and Freundlich (Eqn 5) models, respectively:

$$q_e = \frac{Q_m K_L C_e}{1 + K_L C_e} \qquad (4)$$

$$q_e = K_F C_e^{\frac{1}{n}}, \qquad (5)$$

where K_L (L mg^{-1}) and K_F ((mmol g^{-1})(L mmol^{-1})$^{1/n}$) are the equilibrium constants of Langmuir and Freundlich models, respectively; Q_m (mg g^{-1}) represents the Langmuir adsorption capacity; and n is the variable of adsorption efficiency.

To investigate the effects of pH on adsorption capacity, TC solutions (100 mg L^{-1}) with an initial pH of 3–10 were used. The pH of the suspension was adjusted every 3 h using 0.1 M HCl or NaOH solution (<20 μL per addition) to maintain the initial pH. To reinforce the selective adsorption of TC, 1 mM and 10 mM of cations (Na$^+$, K$^+$, Ca^{2+}, and Mg^{2+}) were chosen for competitive adsorption, which are three and 30 times as high as that of TC, respectively. In addition, to evaluate the re-use performance of the clay minerals, the regeneration capacity was investigated. Upon saturated adsorption of TC at pH 7.0, the adsorbents were regenerated using NaOH solution (pH 11.5). The adsorption-regeneration experiments were repeated five times, and the extent of adsorption was calculated according to Eqn 1.

Characterization methods

Transmission electron microscopy (TEM) images (at 200 kV) of the clay minerals were obtained using a FEI Talos F200S electron microscope. The mineral adsorbent was diluted and uniformly dispersed with deionized water, and one to two drops of suspension was added to the ultra-thin carbon film supported by copper mesh and then dried naturally.

Fourier-transform infrared spectroscopy (FTIR) spectra were recorded on a Bruker Vertex 70 infrared spectrometer (Manheim, Germany). The sample (0.9 mg) was mixed with KBr (~90 mg) and then pressed into a pellet. X-ray diffraction (XRD) patterns were obtained using a Bruker D8 Advance diffractometer (Manheim, Germany). The scanning rate was set at 3°2θ min^{-1} in the range of 3–80°2θ.

Zeta potential and isoelectric point (pH$_{iep}$) were measured on a Zetasizer Nano ZS90 (Malvern Instruments). An appropriate amount of sample was dispersed in 10 mmol L^{-1} KCl solution (solid–liquid ratio of 200 mg L^{-1}) followed by sonication for 5 min to disperse the sample. The prepared suspension was left to stand for 5 min to allow the coarse particles to settle and to obtain a stable suspension. With 0.1 mol L^{-1} KOH and HNO$_3$, the pH range was adjusted to 3–10. Each pH point was measured three times. The size distribution of allophane nanoparticles in suspension was also determined using the Zetasizer Nano ZS90; before measurements, allophane suspension was diluted with deionized water at a concentration of ~200 mg L^{-1}.

The surface site density (D_s) and point of zero net proton charge (pH$_{pzc}$) analyses were conducted at 25°C by acid–base titration using a Metrohm 916 Ti-Touch titrator. HCl (0.1 mol L^{-1}) and NaOH (0.1 mol L^{-1}) solutions were used as titrants with concentrations calibrated by Na$_2$CO$_3$ and potassium hydrogen phthalate, respectively. For titration, 150 mg of the clay mineral was dispersed into 50 mL of deionized water in a 100 mL titration cup. The pH of the suspension was adjusted to ~3 by HCl solution. After 10 min of equilibration, the suspension was slowly back-titrated to pH 11, using an end-point titration (EP) method with NaOH. Each step was stabilized until the pH drift was <0.005 pH unit per minute. Deionized water without samples (blank) was also titrated to deduct the effects of background factors.

N$_2$-physisorption was carried out on a Micromeritics ASAP2020 system at liquid-N$_2$ temperature (–196°C). Before measurement, the sample was degassed at 200°C for 12 h to remove the physically adsorbed water. The specific surface area (S_{BET}) was calculated by the Brunauer–Emmett–Teller (BET) method; the pore size distribution was determined using density functional theory (DFT); the total pore volume (V_{total}) was derived from the N$_2$ uptake amount at a relative pressure of 0.95, and micropore volume (V_{micro}) was evaluated via the *t*-plot method (Thommes et al., 2015).

Results and Discussion

Characteristics of allophane, halloysite, and montmorillonite

TEM results

The TEM images (Fig. 2) revealed directly that allophane, halloysite, and montmorillonite are different in nanostructure dimensions. The allophane showed a hollow sphere diameter of ~5 nm (Fig. 2a), which is in good agreement with the morphological characteristics of natural allophane (Kaufhold et al., 2010). Some aggregates of allophane nanoparticles were also observed, showing a size of submicron to micron scales. Consistent with the above observations, the size distribution of allophane particles also revealed a size range of several nanometers to microns with an average size of 234±9 nm (inset in Fig. 2a). Halloysite showed a nanotubular morphology with a length of 300–700 nm, an inner diameter of 30–100 nm, and an outer diameter of 50–150 nm (Fig. 2b). It is well known that halloysite is a kind of kaolin group mineral with a multiwall nanotube structure, of which the unit
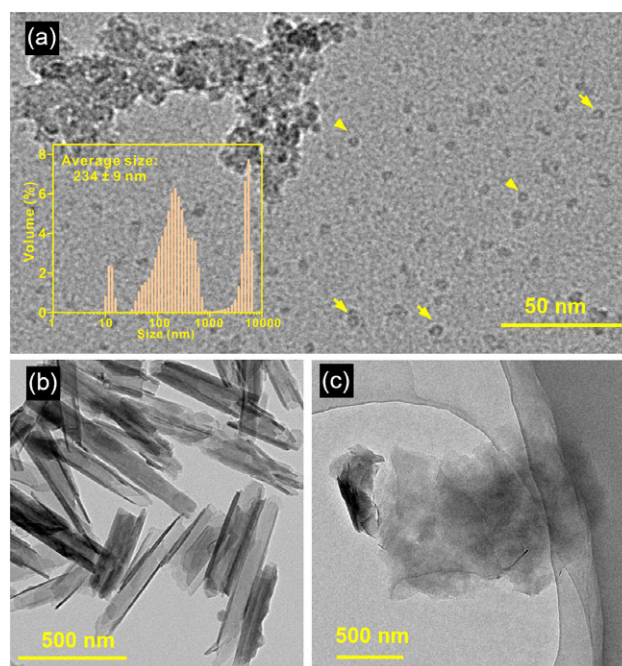
Figure 2. TEM images of (a) allophane (inset shows the size distribution and the yellow arrows indicate the single hollow spherical nanoparticle), (b) halloysite, and (c) montmorillonite.

layers consist of one silica tetrahedral outer sheet and one alumina octahedral inner sheet, i.e. a 1:1 layered nanotubular clay mineral (Yuan et al., 2015). Montmorillonite showed a two-dimensional layer morphology with a size of several micrometers (Fig. 2c), consistent with its typical two-dimensional layered structure. The layer units followed the stacking sequence of tetrahedral-octahedral-tetrahedral sheets, i.e. a 2:1 layered clay mineral (Golubeva, 2016).

XRD pattern analysis

The XRD patterns (Fig. 3) of allophane, halloysite, and montmorillonite revealed the differences in their skeleton structure. Allophane consisted of a major reflection at ~3.4 Å (26° 2θ) with two weak reflections at ~2.3 Å (40°2θ) and ~1.4 Å (66.5°2θ), which are typical characteristics of allophane (Levard et al., 2012). The first reflection is assigned to the constructive interference between adjacent silica tetrahedra, while the latter two reflections arise from the skeleton structure ($(OH)_3Al_2O_3SiOH$, named imogolite-like local structure, ImoLS). Allophane and imogolite are chemically similar and both have imogolite local structure (ImoLS), i.e. fragments formed by the substitution of hydroxyl groups on one side of what appears to be an alumina trihydrate sheet by an isolated protosilicate group leading to its curling. Therefore, allophane and imogolite can be regarded as nanomineral polytypes consisting of the ImoLS units (Wang et al., 2024). One broad reflection at ~11 Å was also observed, which should arise from the long-range order associated with structural water in allophane (Du et al., 2018). The XRD pattern of halloysite showed three main reflections at 7.2 Å (12.3°2θ), 4.4 Å (20.1°2θ), and 3.6 Å (24.8°2θ), corresponding to the (001), (100), and (002) reflections of 7 Å nanotubular halloysite, respectively (Gray-Wannell et al., 2020). The first reflection in the montmorillonite XRD pattern, corresponding to the d_{001} basal spacing, was observed at 12.5 Å (7.02°2θ), suggesting a Na-montmorillonite (Deng et al., 2017). Beyond that, two reflections located at ~3.3 Å (26.6°2θ) and ~3.0 Å (29.4°2θ) are ascribed to quartz and calcite, respectively (Hayati-Ashtiani, 2012). Accordingly, the CaO component as discussed above in relation to XRF data is supposed to arise from the impurity of calcite.

FTIR spectra analysis

The FTIR spectra of allophane, halloysite, and montmorillonite (Fig. 4) also revealed the distinct differences in their structures. The main characteristic bands of allophane were observed as reported previously (Wang et al., 2020). The broad band
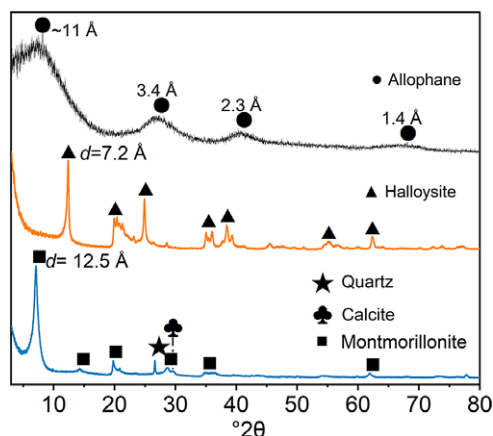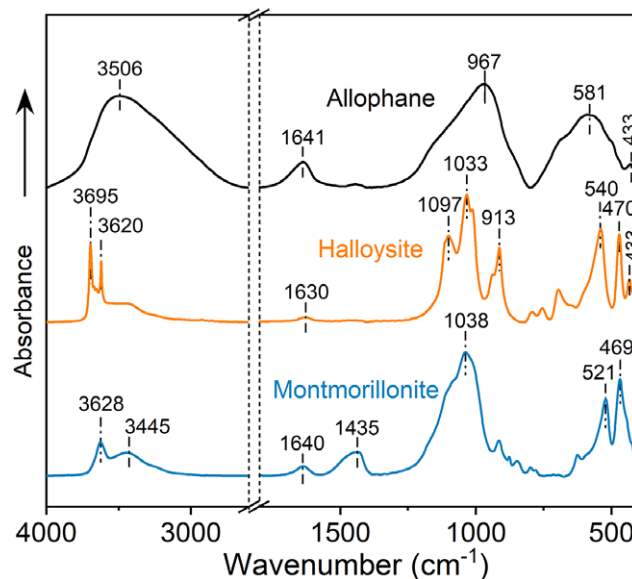

Figure 4. FT-IR spectra of allophane, halloysite, and montmorillonite.

at ~3506 cm^{-1} is ascribed to the -OH stretching vibration in allophane and physically adsorbed water, while the band at 1641 cm^{-1} is ascribed to the H-O-H bending vibration of physically adsorbed water. In the 1200–400 cm^{-1} region, the fingerprint bands of hollow spherical allophane were observed, wherein the primary bands at 967 and 581 cm^{-1} arose from the Si-O-(Al) stretching vibration and the Al octahedra in ImoLS units, respectively (Levard et al., 2012). For halloysite, the 3695 and 3620 cm^{-1} bands belong to the inner-surface and inner Al-OH groups, respectively, and the 913 cm^{-1} band is related to the bending vibration of inner Al-OH groups (Christoforidis et al., 2016). The skeleton structural bands of halloysite were also observed, e.g. 1097, 1033, 540, and 470 cm^{-1} (Yuan et al., 2008). In the spectrum of montmorillonite, the 3628 cm^{-1} band belongs to the stretching vibration of structural hydroxyl groups, while the 3445 and 1636 cm^{-1} bands correspond to the H-O-H stretching and bending vibrations of interlayer water, respectively. The skeleton structural features were observed in the 1200–400 cm^{-1} region as reported previously (He et al., 2004). In addition, the band at ~1435 cm^{-1} is attributed to the carbonate impurities such as calcite as mentioned above (Lu et al., 2016).

N$_2$ physisorption analysis

The N$_2$ adsorption-desorption isotherms and derived power spectral density (PSD) curves of allophane, halloysite, and montmorillonite (Fig. 5), together with the derived textural parameters (Table 2), suggested that these clay minerals have different nanopore structures. According to the IUPAC notations (Thommes et al., 2015), the N$_2$ adsorption-desorption isotherm of allophane (Fig. 5a) is classified as Type-I. The adsorption penetration curve of allophane increased significantly at low relative pressure, and no apparent hysteresis loop was observed, indicating the dominance of micropores in allophane (Cychosz et al., 2017). Indeed, allophane showed a majority of 1–2 nm micropores with a small proportion of 2–3 nm mesopores (Fig. 5b), giving an average pore size of ~1.83 nm (Table 2). The isotherms of halloysite and montmorillonite (Fig. 5c,e) were similar to each other and exhibited Type-II isotherms with type-H3 hysteresis, implying the dominant roles of mesopores and

Figure 3. XRD patterns of allophane, halloysite, and montmorillonite.
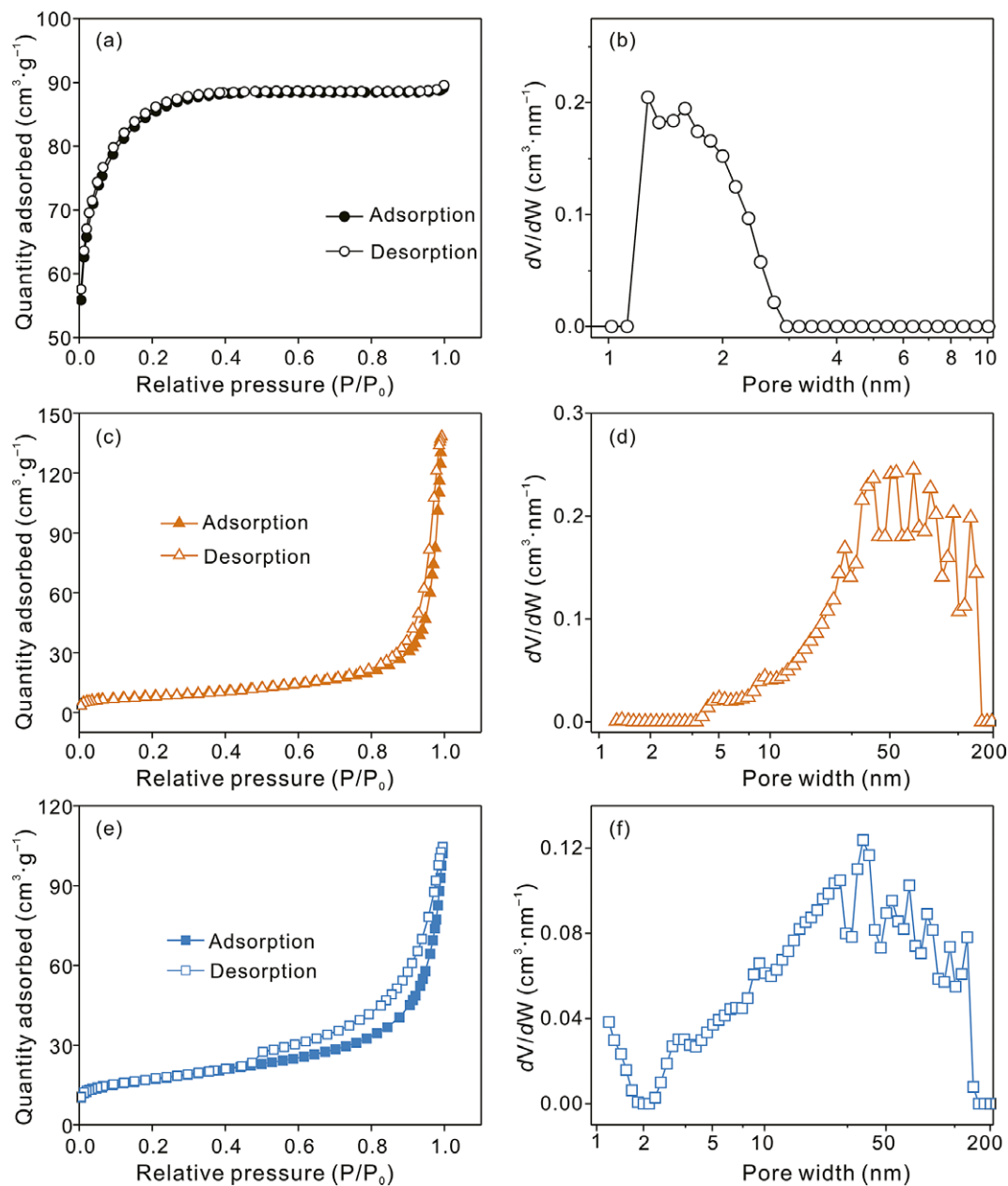
Figure 5. N$_2$ adsorption-desorption isotherms of (a) allophane, (c) halloysite, and (e) montmorillonite; pore-size distributions of (b) allophane, (d) halloysite, and (f) montmorillonite.

Table 2. Textural parameters, pH$_{pzc}$, and surface site densities of samples

Sample	S_{BET} (m^2 g^{-1})	V_{total} (cm^3 g^{-1})	V_{micro} (cm^3 g^{-1})	d_{avg} (nm)	pH$_{PZC}$	H_s (10^{-4} mol L^{-1})	D_s (sites nm^{-2})
Allophane	301	0.14	0.089	1.83	9.6±0.1	20.50±0.09	1.57±0.03
Halloysite	28	0.13	0.001	15.65	7.8±0.2	1.42±0.02	1.02±0.07
Montmorillonite	60	0.11	0.007	12.86	9.8±0.1	12.57±0.06	4.20±0.10

d_{avg} = average pore width; pH$_{PZC}$ = point of zero net proton charge; H_s = total surface proton concentration; D_s = surface site density. The values were calculated by Eqn 12 using S_{BET} and H_s.

macropores (Thommes et al., 2015), consistent with their PSD curves (Fig. 5d,f). Correspondingly, the average pore sizes of both minerals were 15.65 and 12.86 nm, respectively, which are much larger than those of allophane. As is well known, the nanopores of the halloysite mainly consisted of mesopores and macropores, which are often evaluated by using the BJH method (suitable for nanopores with a diameter of >2 nm) (Liu et al., 2008; Song et al., 2020). In the present work, the DFT method, which is all-powerful

and suitable for evaluation of micropores and macropores (Thommes et al., 2015), was used to evaluate the pore-size distribution of halloysite for a better comparison study. Although some differences were observed in the pore-size distribution curves between current work and previous reports (Liu et al., 2008) due to the employment of different fitting models, all of the pore-distribution curves showed the predominant position of mesopores and macropores in halloysite, without micropores (<2 nm).

Note that the interlayers of montmorillonite were filled with guests (e.g. water, cations) (Macht et al., 2011) and that N_2 adsorption is kinetically limited in pores of <0.5 nm in diameter (Pereira et al., 2019). As a consequence, the S_{BET} of montmorillonite (60 m^2 g^{-1}) was considered to be much lower than its real value. By comparison, the S_{BET} and nanopores of halloysite can be detected by N_2 adsorption-desorption, due to its inner diameter being ~30–100 nm (Fig. 2b). In addition, the V_{total} (0.14 cm^3 g^{-1}) and S_{BET} (301 m^2 g^{-1}) of allophane (freeze-dried powder) (Table 2) were considered to be much less than its theoretical values (Abidin et al., 2006), implying that allophane nanoparticles aggregated to a significant extent during the drying process. Overall, allophane has a much larger S_{BET} value than halloysite and montmorillonite, resulting from its relatively large proportion of micropores. Therefore, nano hollow spherical allophane was expected to exhibit better N_2 adsorption performance than halloysite and montmorillonite.

Surface charge property

The zeta potential curves and acid–base titration data of allophane, halloysite, and montmorillonite (Fig. 6) were obtained to reveal their surface-charge properties. With the increase in pH, the surfaces of these minerals became more negative. The pH_{iep} of allophane was ~9 and had a positively charged surface over a wide pH range, while halloysite and montmorillonite showed negatively charged surfaces over the measured pH range (3–10); these results are consistent with previously reported data (Cui et al., 2020; Melnikov et al., 2023; Wang et al., 2024). Because the deprotonation of Si-OH groups via ionization is easier than that of Al-OH under higher pH conditions (Arancibia-Miranda et al., 2015), allophane with abundant Al-OH groups on its outer surface should logically have a higher pH_{pzc} than either halloysite or montmorillonite. The outer surface of halloysite is a relatively less reactive Si-OH group with a negative charge, whereas the outer surface of allophane is perhaps a relatively more reactive Al-OH group with a positive charge. Moreover, the tricarbonyl system and the phenol diketone portion of the TC molecule readily isolate some of the protons from water, and the tetracycline exists as either a monovalent anion or a divalent anion. As a result, allophane is favorable for capturing negatively charged species, while halloysite and montmorillonite are more likely to attract positively charged species.

Surface hydroxyl groups are essential to surface reactions occurring at the mineral–water interface, which can be determined by acid–base
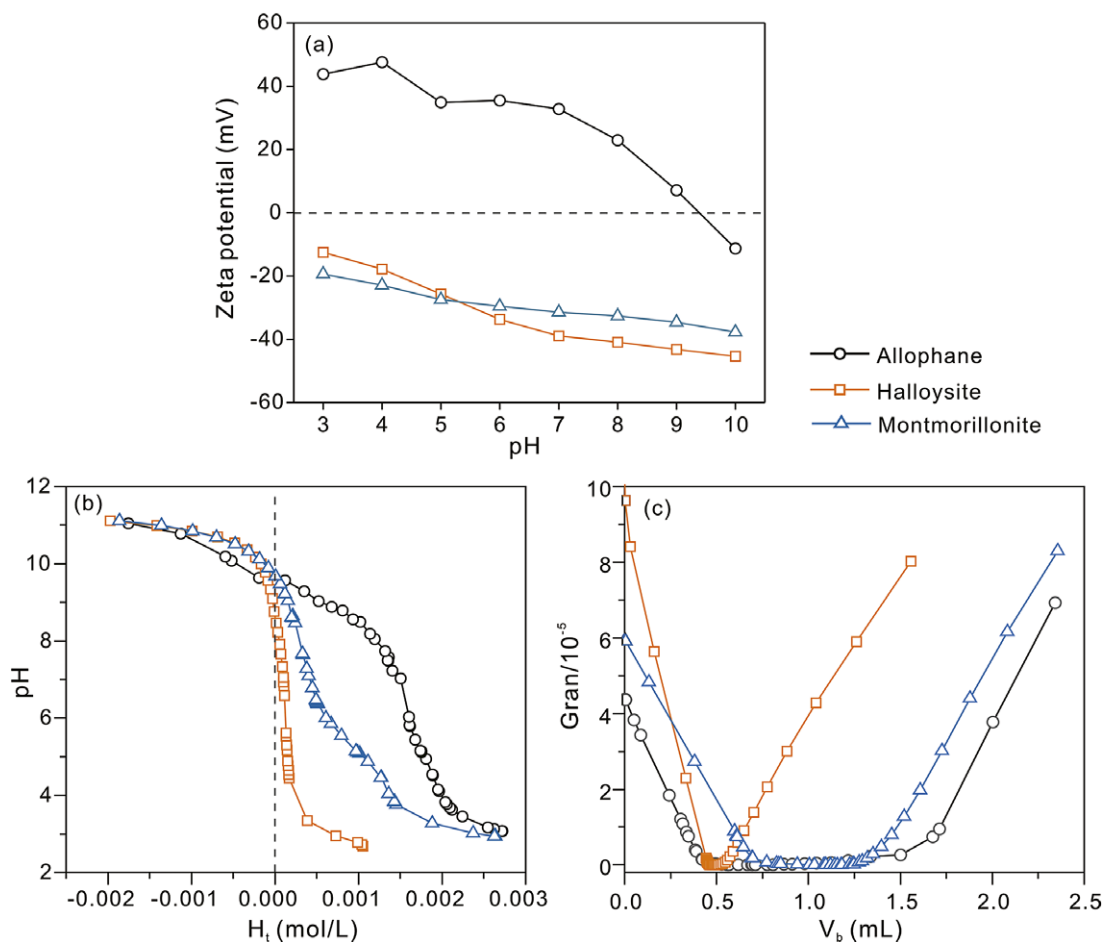
Figure 6. (a) Zeta potential curves, (b) acid–base titration curves in deionized water, and (c) Gran plots of titration data to obtain V_{eb1} and V_{eb2} (see text for notation) of the clay minerals.

titration. The acid–base titration results of allophane, halloysite, and montmorillonite (Fig. 6b,c) were obtained, from which some parameters (Table 2) were also derived. H_t represents the total proton concentration and is defined as (Nie et al., 2013):

$$H_t = [H^+] - [OH^-] + [\equiv SOH_2^+] - [\equiv SO^-] \tag{6}$$

$$[\equiv SOH] + H^+ \leftrightarrow [\equiv SOH_2^+] \tag{7}$$

$$[\equiv SOH] \leftrightarrow H^+ + [\equiv SO^-] \tag{8}$$

where $[H^+]$ and $[OH^-]$ represent the concentrations of proton and hydroxide ions in solution, respectively; and $[\equiv SOH_2^+]$ and $[\equiv SO^-]$ represent the protonated and deprotonated species of surface hydroxyl groups on clay minerals (Eqns 7 and 8), respectively. The H_t can be calculated from the difference between protons added during the titration and protons remaining in solution (Eqn 9):

$$H_t = (C_a V_a - C_b V_b)/(V_0 + V_a + V_b), \tag{9}$$

where C_a and C_b (mol L^{-1}) are the calibrated concentrations of HCl and NaOH solutions; and V_0 (L), V_a (L), and V_b (L) are the volumes of initial deionized water, consumed HCl solution, and consumed NaOH solution, respectively.

The pH$_{pzc}$ refers to the pH value where the total net proton charge on the mineral surface is zero, which is useful for predicting the electrostatic attraction of charged species in aqueous solution. The pH$_{pzc}$ of allophane (~9.6; Fig. 6b and Table 2) was higher than those (5–8) of natural allophane samples (Diez et al., 2005), which may result from the impurities in natural allophane. The pH$_{pzc}$ values of halloysite and montmorillonite were ~7.8 and ~9.8, consistent with those reported previously (Tombacz and Szekeres, 2004). Note that the pH$_{pzc}$ values of these clay minerals were higher than their pH$_{iep}$ values, which can be attributed to the isomorphic substitutions in their structures, e.g. the replacement of Al^{3+} by Mg^{2+} in octahedral sites and Si^{4+} by Al^{3+} in tetrahedral sites (Yucelen et al., 2012; Golubeva, 2016; Yu et al., 2020). Nanoscale pore confinement may also cause an increase in the pH$_{pzc}$ of halloysite, due to the deviation of surface chemistry of aluminum groups in the nanopores (Yu et al., 2020).

The surface site density of clay minerals can be determined by the Gran equations (Eqns 10 and 11) (Yu et al., 2020):

$$Gran = (V_0 + V_a + V_b) \times 10^{-pH}, \text{for pH} < 7.0 \tag{10}$$

$$Gran = (V_0 + V_a + V_b) \times 10^{(pH + \log K_w)}, \text{for pH} > 7.0 \tag{11}$$

where V_0, V_a, and V_b are the same as those in Eqn 9; K_w is the ionic product of water, which is −13.93 (25°C) here (Bujnakova et al., 2013). The value of Gran was plotted *vs* the added volume of NaOH solution (Fig. 6c), then the curves were fitted with two lines, yielding two intersections with the *x*-axis at V_{eb1} and V_{eb2}. The total proton concentration (H_s, mol L^{-1}) was calculated as follows (Eqn 12):

$$H_s = [(V_{eb2} - V_{eb1})C_b - (V_{eb2-blank} - V_{eb1-blank})C_b]/V_0 \tag{12}$$

and the surface site density (D_s, sites nm^{-2}) was calculated by Eqn 13:

$$D_s = (H_s N_A)/(S C_s 10^{18}) \tag{13}$$

where $V_{eb2-blank}$ and $V_{eb1-blank}$ are derived from the Gran function of deionized water (blank); N_A is Avogadro's constant, 6.02×10^{23} mol^{-1}; S (m^2 g^{-1}) is the specific surface area of samples, and in this study the S_{BET} was used; and C_s (g L^{-1}) is the sample dosage.

The H_s values of the clay minerals (Table 2) followed the order allophane > montmorillonite > halloysite. However, the D_s of montmorillonite was much greater than that of allophane, not to mention that of halloysite. This can be explained by the same explanation as given above, i.e. the S_{BET} of montmorillonite is much lower than its true value because only the external specific surface area is measured by N$_2$ molecules, whereas the interlayer space of montmorillonite is accessible for H$^+$ (Cui et al., 2020), thus causing an extremely high D_s value.

Adsorption performances of allophane, halloysite, and montmorillonite

Effects of pH
Adsorption data under various pH conditions showed that the pH had great effects on the adsorption capacity of the clay minerals (Fig. 7). The uptake amount of TC increased at first and then decreased, which should be related to both the surface charge properties of the clay minerals and the forms of TC. Under strong acidic conditions, electrostatic repulsion existed between cationic TC molecules and positive allophane surfaces (Figs 1 and 6a). With the increase of pH, TC molecules became more negative, which promoted its adsorption on positive allophane surfaces (pH<9) but suppressed its adsorption on negative allophane surfaces (pH>9). Consequently, allophane gave a maximal adsorption amount of 796 mg g^{-1} at pH 9. In the same way, at pH<7.7, the cationic and/or zwitterionic TC species were more favorable to be adsorbed on negatively charged halloysite and montmorillonite at conditions with higher pH, giving maximal adsorption amounts of 83 and 225 mg g^{-1} at about pH 7 for halloysite and montmorillonite, respectively. Similar results have been reported for the effects of pH on tetracycline adsorption on clay minerals (Liu et al., 2012). These results suggest that electrostatic attraction is the primary driving force.
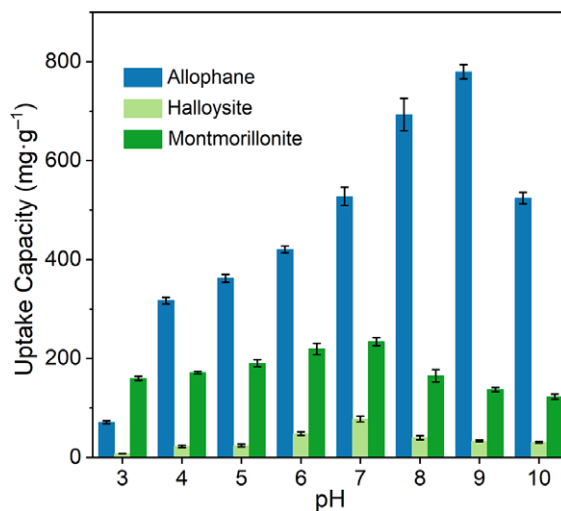
**Figure 7.** The effect of pH on the adsorption performance of clay minerals (adsorbent dosage, 5 mg; TC, 50 mL and 100 mg L^{-1}).

Influence of co-existing ions and ionic strength

The effects of co-existing cations (Na$^+$/K$^+$/Mg^{2+}/Ca^{2+}) and their strength (1 mM/10 mM) on TC adsorption (Fig. 8) were evaluated. The adsorption capacities of allophane and halloysite were affected little in the presence of Na$^+$ and K$^+$, implying the dominant role of inner-sphere complexation in TC adsorption on both clay minerals (Su et al., 2010). As TC can form inner-sphere complexes with hydrous oxides of Al via ligand exchange (Gu and Karthikeyan, 2005), such an interaction might also occur between TC and surface Al-OH groups of clay minerals. In addition, TC adsorption on allophane decreased in the presence of Mg^{2+} and Ca^{2+}. One possible explanation is that divalent Mg^{2+} and Ca^{2+} can form metal complexes with TC molecules to reduce the free concentration of TC in the solution (Pulicharla et al., 2017). For montmorillonite, the adsorption capacity decreased with increasing cationic strength, suggesting that non-specific adsorption mainly occurred. Moreover, the inhibiting effects of divalent cations (Mg^{2+} and Ca^{2+}) on adsorption performance were relatively weak, consistent with what has been reported previously (Aristilde et al., 2016). It is attributed to the formation of ternary complexes mediated by the bridge role of divalent cations in the interlayer spaces (entering via cation exchange) of montmorillonite.

The values of D_s and S_{BET} of allophane were much greater than those of halloysite and montmorillonite (Table 2), and meanwhile the external surfaces of halloysite and montmorillonite had Si-O-Si bonds and Si-O- defect sites, in which the TC species are thought to be physically bonded (Qiao et al., 2021). One, therefore, could reasonably conclude that allophane exhibits the best performance for TC adsorption, which strongly suggests that allophane is a promising adsorbent for TC removal.

Adsorption kinetics

The adsorption kinetics of TC on allophane, halloysite, and montmorillonite (Fig. 9) showed that these adsorption processes were very fast at the beginning (<240 min) and then slowed down until equilibrium, giving an adsorption capacity
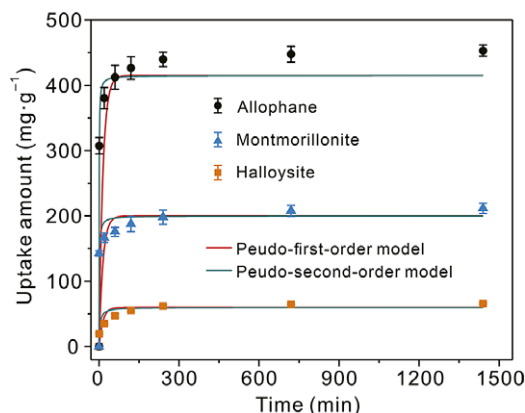

Figure 9. Adsorption kinetics of allophane, halloysite, and montmorillonite (adsorbent dosage, 5 mg; TC, 50 mL and 100 mg L^{-1}; equilibrium pH, ~7.0).

order of allophane > montmorillonite > halloysite. The kinetic data were fitted by the pseudo-first order and pseudo-second order models (Eqns 2–3), respectively. Results showed that the latter model better described the adsorption process (Fig. 9 and Table 3), suggesting that surface complexation may take a dominant position.

Adsorption isotherms

The adsorption isotherms of TC (Fig. 10) were obtained and showed that the equilibrium uptake capacities (q_e) of these minerals increased with the equilibrium concentration (C_e). To better understand the adsorption mechanisms, the isothermal data were fitted with the Langmuir and Freundlich models, and the fitting results are summarized in Table 4. Based on the coefficient of regression (R^2) values, the Langmuir model was better for predicting isothermal data than the Freundlich model. These results imply that all adsorption sites are energetically equivalent and that TC adsorption on these clay minerals is more
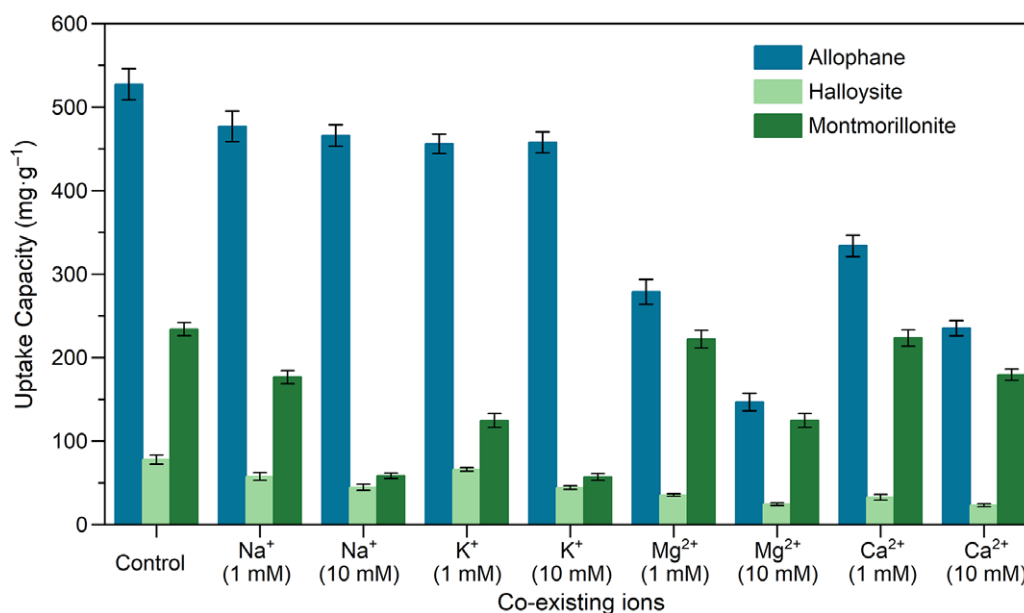
Figure 8. Effects of ion strength on the adsorption properties of clay minerals (adsorbent dosage, 5 mg; TC, 50 mL and 100 mg L^{-1}; equilibrium pH was set at ~7.0).

Table 3. Pseudo-first order and pseudo-second order adsorption kinetics parameters

Samples	Pseudo-first order model			Pseudo-second order model		
	K_1 (min^{-1})	$q_{e\,(1Cal.)}$ (mg g^{-1})	R^2	K_2 (g mg^{-1} min^{-1})	$q_{e\,(2Cal.)}$ (mg g^{-1})	R^2
Allophane	1.293	424	0.977	0.0056	430	0.980
Halloysite	0.036	60	0.891	0.0014	65	0.918
Montmorillonite	1.265	199	0.942	0.0139	193	0.951

Table 4. Langmuir and Freundlich adsorption isotherm fitting parameters

Samples	Langmuir model			Freundlich model		
	K_L (L·mg^{-1})	q_m (mg g^{-1})	R^2	K_F (mmol g^{-1})(L mmol^{-1})$^{1/n}$	n	R^2
Allophane	0.074	541	0.986	85.65	2.39	0.970
Halloysite	0.006	193	0.983	2.04	1.27	0.974
Montmorillonite	0.013	458	0.991	12.75	1.50	0.989
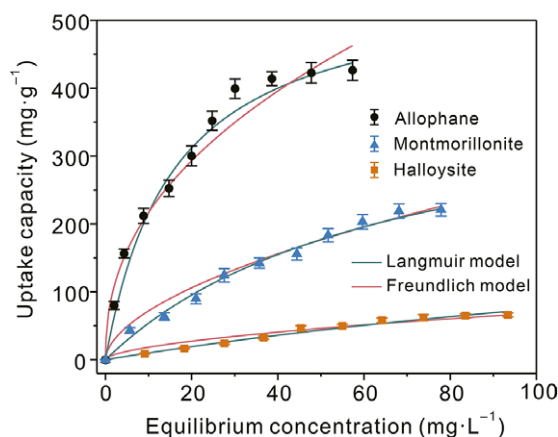
Figure 10. Adsorption isotherms of allophane, halloysite, and montmorillonite (dosage, 5 mg; TC, 50 mL and 100 mg L^{-1}; equilibrium pH ~ 7.0).

Figure 11. Regeneration and reusability of allophane, halloysite, and montmorillonite (adsorbent dosage, 5 mg; TC, 50 mL and 100 mg L^{-1}; equilibrium pH ~ 7.0).
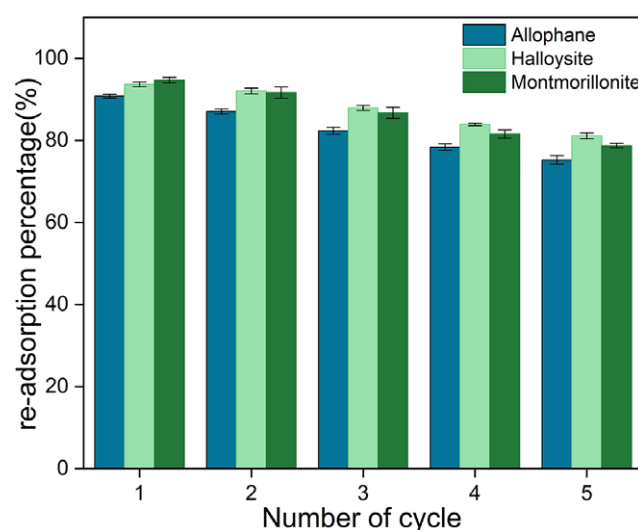
likely to be monolayer adsorption, which depends on the available active sites on the mineral surface (Obradovic, 2020).

Regeneration and re-usability

The adsorption data of regenerated clay minerals were also obtained (Fig. 11); a dilute NaOH solution with a pH of 11.5 was used to regenerate the adsorbents. After five cycles, the adsorption capacities of all adsorbents were maintained at >75%, implying that these three adsorbents had good re-usability and stability in the regeneration process. Furthermore, although the adsorption efficiency showed an order of halloysite > montmorillonite > allophane, the initial adsorption capacity of allophane is much higher than that of halloysite and montmorillonite. These results highlight the huge potential application of allophane in TC removal.

Adsorbent performances for TC uptake from aqueous media

The adsorption effectiveness for antibiotics depends mainly on the adsorbents' structure and properties, such as specific surface area and surface-interface properties. The adsorption capacities of these clay minerals with different nanostructures in this study were compared with the materials widely used for TC removal (Table 5).

Allophane has a greater adsorption capacity for TC than materials reported in most literature. With an increased interest in nanomaterials, eco-friendly and inexpensive clay minerals, especially hollow spherical allophane, would be a preferred candidate for chemically synthesized nanomaterials.

Adsorption mechanisms of TC on three clay minerals

XRD patterns

After TC adsorption, the XRD patterns of TC-adsorbed allophane, halloysite, and montmorillonite (Fig. 12) were recorded. Compared with the spectra of raw minerals, the reflections of allophane and halloysite remained almost constant, demonstrating that TC molecules were adsorbed on the surface sites of both minerals and had no significant effect on their skeleton structures. Given that the reflection at 11 Å (8°2θ) is related to some long-range order of structural water in allophane, its disappearance after adsorption should result from the inner-sphere complexation of TC with
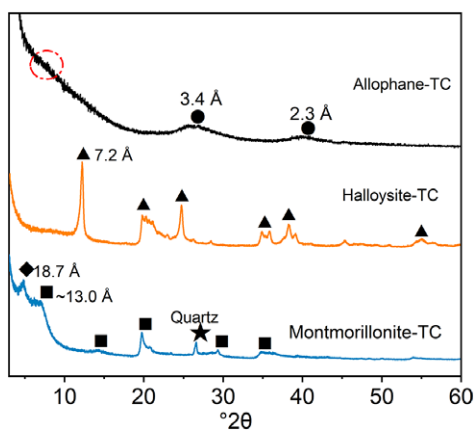
Figure 12. XRD patterns of allophane, halloysite, and montmorillonite after TC adsorption.

Table 5. Comparison of adsorption capacities of various media for TC

Adsorbent	q_m (mg g^{-1})	Adsorption model	References
Kaolinite	2.3	Langmuir	Li et al. (2010)
Illite	32	Elovich	Chang et al. (2012)
ZnCl$_2$-treated biochar	93	Langmuir	Yan et al. (2020)
Palygorskite	320	Langmuir	Wang et al. (2019)
Zeolite-A-MCM–41	419	Langmuir	Liu et al. (2013)
UiO–67 (3D MOF)	427	Langmuir	Yang et al. (2020)
DDMGO	1200	Freundlich	Li et al. (2018)
TDMGO	1233	Langmuir	Yang et al. (2017)
Halloysite	193	Langmuir	This study
Montmorillonite	458	Langmuir	This study
Allophane	796	Langmuir	This study

allophane Al-OH sites, which can readily expel the water molecules from around the outer surface of the allophane. For montmorillonite, the d_{001} value shifted from 12.4 Å to 18.7 Å, which is consistent with the XRD results reported previously, and is attributed to the intercalation of TC in the interlayer spaces (Wu et al., 2019). Despite that, some interlayer spaces of Na-montmorillonite were not occupied, as indicated by a shoulder reflection at ~13 Å (6.7°2θ).

FTIR results of clay minerals after TC adsorption

After TC adsorption, the FTIR spectra of allophane, halloysite, and montmorillonite after TC adsorption (Fig. 13a) were also obtained. Because the fingerprint bands of TC are mainly in the wavenumber range of 1400–1700 cm^{-1} (Zhang et al., 2015; Li et al., 2017), the FTIR spectra in this region were magnified (Fig. 13b). Compared with the spectra of raw minerals (Fig. 4), several bands related to TC molecules appeared in those of adsorption products, together with shifts in some bands, which demonstrated the interactions between TC molecules and clay minerals.

In the spectrum of allophane-TC, the broad band at ~3472 cm^{-1} is attributed to the overlapping of the 3506 cm^{-1} band of allophane and the 3391 cm^{-1} band of TC, implying a mass of adsorbed TC on allophane. After adsorption, the structural bands of allophane

(967 and 578 cm^{-1}) shifted several wavenumbers (to 970 and 568 cm^{-1}, respectively), and meanwhile, the bands assigned to -C=O and -NH$_2$ groups of TC were not observed or overlapped with other bands. These results demonstrate that the -C=O and -NH$_2$ groups of TC were strongly bound with the surface Al-OH groups of allophane, which is in agreement with the inner-sphere adsorption of TC on allophane as discussed above. The strong interactions may also affect the skeleton vibration of the TC molecule greatly, which shifted the 1454 cm^{-1} band of TC to about 1466 cm^{-1} after adsorption.

Because the inner Al-OH groups of halloysite cannot be reached by organic molecules (Yuan et al., 2008), its signal intensity (3620 or 913 cm^{-1}) can be used as an internal reference for comparing band intensities. Following that, the relative intensities of 3695 and 1033 cm^{-1} of halloysite decreased after TC adsorption, suggesting the interactions of TC species with Al-OH and Si-O groups, respectively. Similar results have been reported for oxytetracycline (OTC) adsorption on halloysite (Ramanayaka et al., 2020). The characteristic bands of TC in the 1700–1400 cm^{-1} region were identified with slight shifts, implying that TC species were mainly adsorbed via outer-sphere complexation that had no significant change in TC structure. As the Si-OH groups on the defect sites of halloysite are deprotonated under weakly acidic to alkaline conditions (Tan et al., 2016), it can be speculated that TC species mainly formed inner-sphere complexes with Al-OH groups at inner surfaces but electrostatically adsorbed on the negatively charged external surface.

Concerning montmorillonite-TC, its FTIR spectrum is comparable to that of raw montmorillonite, which is consistent with the results of previous studies (Parolo et al., 2008; Ortiz-Ramos et al., 2022). The structural bands of TC were also observed; the band at 1620 cm^{-1} was attributed to the overlap of the TC bands and interlayer water, and the 1500 cm^{-1} band may arise from the shifted -NH$_2$ amide groups of TC (1517 cm^{-1}). Combined with XRD results, it can be inferred that the intercalation of TC into the interlayer spaces of montmorillonite made no significant change in the skeleton structure of TC and montmorillonite.

TC adsorption mechanisms

As discussed above, the nanostructure of clay minerals has a great effect on their specific surface areas, nanopore structures, and surface charge properties, thereby significantly limiting their adsorption performance and interaction mechanism with TC species. The possible adsorption mechanisms of TC on allophane, halloysite, and montmorillonite are illustrated in Fig. 14. Owing to its unique hollow spherical structure, allophane has the largest specific surface area compared with halloysite and montmorillonite, together with plenty of hydroxyl groups on the surface and near the defect pores. Consequently, allophane exhibited the largest adsorption capacity to TC species (796 mg g^{-1}), which was dominated by ligand exchange with Al-OH groups, forming inner-sphere complexes. Such an inner-sphere complexation is thought to occur at the inner surfaces with many Al-OH groups of halloysite nanotubes, due to the lumen diameter being much larger than the TC molecule. In addition, allophane and halloysite also contain some Si-OH groups at the defect sites and/or structural edges, which appear in deprotonated form (Si-O$^-$) in most pH cases. Therefore, some cationic TC species may also be electrostatically attracted by the negatively charged Si-O$^-$ sites. For montmorillonite with an expandable layered structure, cation exchange is the main mechanism for TC
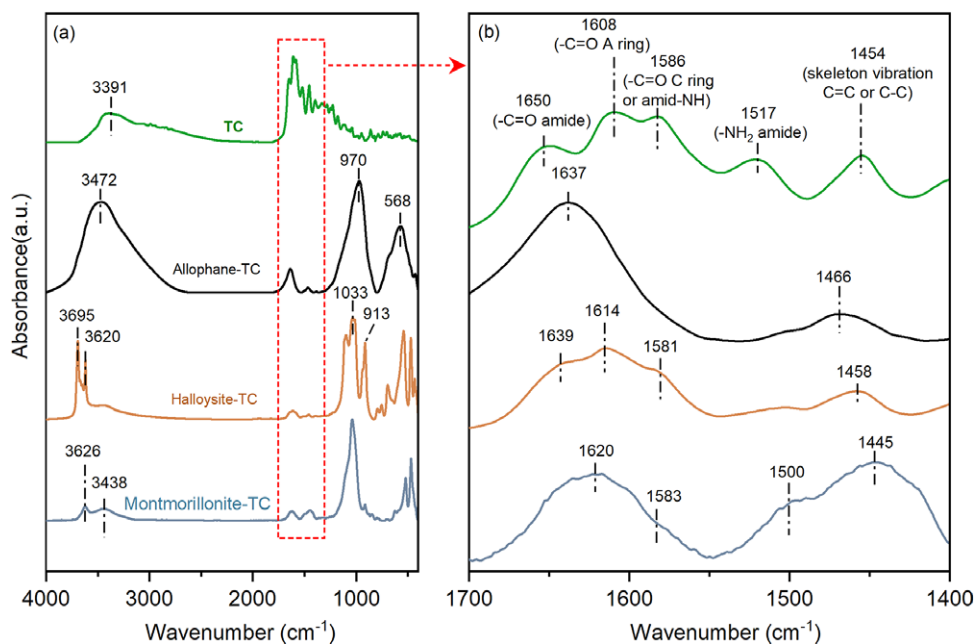
Figure 13. (a) FTIR spectra of allophane, halloysite, and montmorillonite after TC adsorption; (b) enlargement of the section of the FTIR spectra as indicated by the red dashed line in part a.
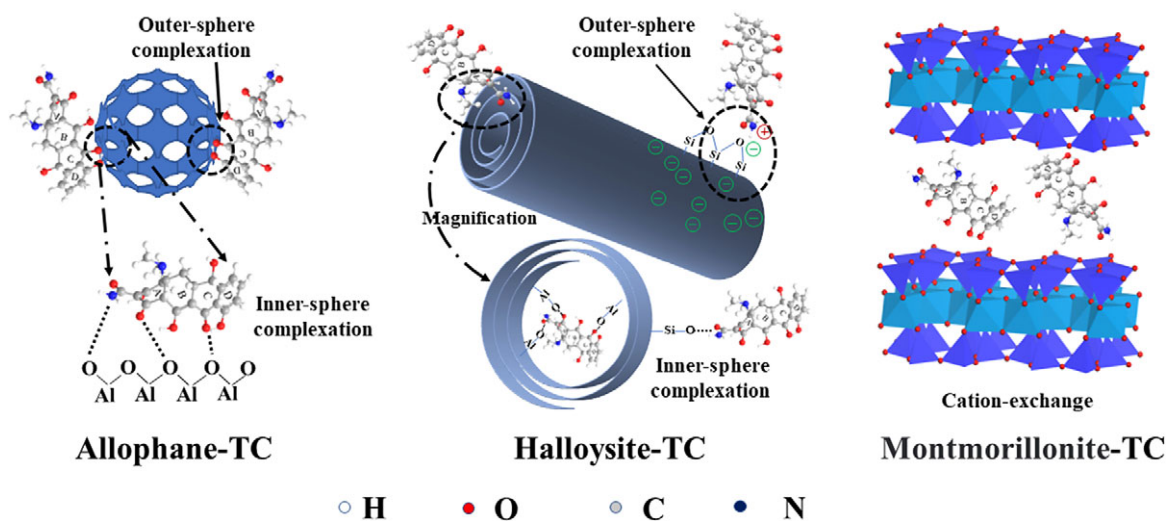
Figure 14. Illustration of main the adsorption mechanisms of TC on three clay minerals with different nanostructures.

adsorption, which could increase the interlayer space but barely change the skeleton structure of the TC species and montmorillonite.

Summary and conclusions

In summary, the adsorption of TC on allophane, halloysite, and montmorillonite, which have varying nanostructures, was compared. The nanostructural features and surface physicochemical properties of these clay minerals were characterized systematically via a combination of techniques, i.e. TEM, XRD, FTIR, zeta potential, N_2-physisorption, acid–base titration, etc. The adsorption processes of TC on these three minerals were best described by pseudo-second order kinetics and Langmuir models. These clay minerals performed better under neutral to weakly alkaline conditions, and by comparison, the adsorption capacity of allophane reached 796 mg g^{-1}, which was much greater than those of halloysite and montmorillonite. In addition, these minerals still had large adsorption capacities in the presence of Na$^+$/K$^+$/Ca^{2+}/Mg^{2+} and maintained remarkable efficiencies, exceeding 75% after five recycles. Furthermore, some changes were observed in the surface groups and nanostructures of the clay minerals, and combined with the adsorption behaviors, the adsorption mechanisms were proposed. Driven by electrostatic forces, the inner-sphere complexation of TC with Al-OH groups dominated its adsorption on the external surface of allophane and the halloysite inner surfaces, accompanied by electrostatic attraction between a small amount of cationic TC species and Si-O$^-$ sites, while the TC adsorption on montmorillonite was dominated by cation exchange in the interlayer spaces. This study provides a better understanding of the effects of nanostructures of clay

minerals on their TC adsorption performances and strongly suggests that allophane is a promising inexpensive adsorbent for the efficient removal of TC from wastewater.

Author contributions. Qiyi Ma: Conceptualization, Writing original draft, Data curation, Formal analysis. **Ning Zhao:** Validation, Data Curation. **Shun Wang:** Supervision, Conceptualization, Writing-review & editing, Project administration, Funding acquisition. **Baifa Zhang:** Methodology, Data Curation. **Mengyuan Li:** Methodology, Data Curation. **Dong Liu:** Supervision, Formal analysis. **Xiang Zhou:** Formal analysis. **Maxim Rudmin:** Writing-review & editing. **Antoine F. Mulaba-Bafubiandi:** Writing-review & editing. **Peng Yuan:** Supervision, Writing-review & editing.

References

Abidin, Z., Matsue, N., & Henmi, T. (2006). Validity of proposed model for the chemical structure of allophane with nano-ball morphology. *Clay Science*, *12*, 267–269.

Arancibia-Miranda, N., Silva-Yumi, J., & Escudey, M. (2015). Effect of cations in the background electrolyte on the adsorption kinetics of copper and cadmium and the isoelectric point of imogolite. *Journal of Hazardous Materials*, *299*, 675–684.

Aristilde, L., Lanson, B., Miehe-Brendle, J., Marichal, C., & Charlet, L. (2016). Enhanced interlayer trapping of a tetracycline antibiotic within montmorillonite layers in the presence of Ca and Mg. *Journal of Colloid and Interface Science*, *464*, 153–159.

Bansal, O.P. (2013). Sorption of tetracycline, oxytetracycline, and chlortetracycline in illite and kaolinite suspensions. *ISRN Environmental Chemistry*, *2013*, 694681.

Bujnakova, Z., Balaz, P., Zorkovska, A., Sayagues, M.J., Kovac, J., & Timko, M. (2013). Arsenic sorption by nanocrystalline magnetite: an example of environmentally promising interface with geosphere. *Journal of Hazardous Materials*, *262*, 1204–1212.

Chang, P.H., Li, Z., Jean, J.S., Jiang, W.T., Wang, C.J., & Lin, K.H. (2012). Adsorption of tetracycline on 2:1 layered non-swelling clay mineral illite. *Applied Clay Science, 67–68*, 158–163.

Christoforidis, K.C., Melchionna, M., Montini, T., Papoulis, D., Stathatos, E., Zafeiratos, S., Kordouli, E., & Fornasiero, P. (2016). Solar and visible light photocatalytic enhancement of halloysite nanotubes/g-C_3N_4 heteroarchitectures. *RSC Advances*, *6*, 86617–86626.

Cui, J., Zhang, Z., & Han, F. (2020). Effects of pH on the gel properties of montmorillonite, palygorskite and montmorillonite-palygorskite composite clay. *Applied Clay Science*, *190*, 105543.

Cychosz, K.A., Guillet-Nicolas, R., García-Martínez, J., & Thommes, M. (2017). Recent advances in the textural characterization of hierarchically structured nanoporous materials. *Chemical Society Reviews*, *46*, 389–414.

Deng, L.L., Yuan, P., Liu, D., Annabi-Bergaya, F., Zhou, J.M., Chen, F.R., & Liu, Z.W. (2017). Effects of microstructure of clay minerals, montmorillonite, kaolinite and halloysite, on their benzene adsorption behaviors. *Applied Clay Science*, *143*, 184–191.

Diez, M.C., Quiroz, A., Ureta-Zañartu, S., Vidal, G., Mora, M.L., Gallardo, F., & Navia, R. (2005). Soil retention capacity of phenols from biologically pre-treated kraft mill wastewater. *Water, Air, and Soil Pollution*, *163*, 325–339.

Du, P., Thill, A., Yuan, P., Wang, S., Liu, D., Gobeaux, F., Deng, L., & Song, Y. (2020). Tailoring structure and surface chemistry of hollow allophane nanospheres for optimization of aggregation by facile methyl modification. *Applied Surface Science*, *510*, 145453.

Du, P., Yuan, P., Liu, D., Wang, S., Song, H., & Guo, H. (2018). Calcination-induced changes in structure, morphology, and porosity of allophane. *Applied Clay Science*, *158*, 211–218.

Ewis, D., Ba-Abbad, M.M., Benamor, A., & El-Naas, M.H. (2022). Adsorption of organic water pollutants by clays and clay minerals composites: a comprehensive review. *Applied Clay Science*, *229*, 106686.

Feng, K., Hung, G.-Y., Yang, X., & Liu, M. (2019). High-strength and physical cross-linked nanocomposite hydrogel with clay nanotubes for strain sensor and dye adsorption application. *Composites Science and Technology*, *181*, 107701.

Golubeva, O.Y. (2016). Effect of synthesis conditions on hydrothermal crystallization, textural characteristics and morphology of aluminum-magnesium montmorillonite. *Microporous and Mesoporous Materials*, *224*, 271–276.

Gopal, G., Alex, S.A., Chandrasekaran, N., & Mukherjee, A. (2020). A review on tetracycline removal from aqueous systems by advanced treatment techniques. *RSC Advances*, *10*, 27081–27095.

Gray-Wannell, N., Holliman, P.J., Greenwell, H.C., Delbos, E., & Hillier, S. (2020). Adsorption of phosphate by halloysite (7 Å) nanotubes (HNTs). *Clay Minerals*, *55*, 184–193.

Gu, C., & Karthikeyan, K.G. (2005). Interaction of tetracycline with aluminum and iron hydrous oxides. *Environmental Science & Technology*, *39*, 2660–2667.

Hayati-Ashtiani, M. (2012). New insights to characterize mineralogical and physicochemical properties of nanoporous and nanostructured bentonites (montmorillonites). *Particulate Science and Technology*, *30*, 474–481.

He, H., Ray, F.L., & Zhu, J. (2004). Infrared study of HDTMA$^+$ intercalated montmorillonite. *Spectrochimica Acta. Part A: Molecular and Biomolecular Spectroscopy*, *60*, 2853–2859.

Huang, Y.-T., Lowe, D.J., Churchman, G.J., Schipper, L.A., Cursons, R., Zhang, H., Chen, T.-Y., & Cooper, A. (2016). DNA adsorption by nanocrystalline allophane spherules and nanoaggregates, and implications for carbon sequestration in Andisols. *Applied Clay Science*, *120*, 40–50.

Kaufhold, S., Dohrmann, R., Abidin, Z., Henmi, T., Matsue, N., Eichinger, L., Kaufhold, A., & Jahn, R. (2010). Allophane compared with other sorbent minerals for the removal of fluoride from water with particular focus on a mineable Ecuadorian allophane. *Applied Clay Science*, *50*, 25–33.

Kulshrestha, P., Giese, R.F., & Aga, D.S. (2004). Investigating the molecular interactions of oxytetracycline in clay and organic matter: insights on factors affecting its mobility in soil. *Environmental Science & Technology*, *38*, 4097–4105.

Leichtweis, J., Vieira, Y., Welter, N., Silvestri, S., Dotto, G.L., & Carissimi, E. (2022). A review of the occurrence, disposal, determination, toxicity and remediation technologies of the tetracycline antibiotic. *Process Safety and Environmental Protection*, *160*, 25–40.

Levard, C., Doelsch, E., Basile-Doelsch, I., Abidin, Z., Miche, H., Masion, A., Rose, J., Borschneck, D., & Bottero, J.Y. (2012). Structure and distribution of allophanes, imogolite and proto-imogolite in volcanic soils. *Geoderma*, *183*, 100–108.

Li, M.F., Liu, Y.G., Liu, S.B., Zeng, G.M., Hu, X.J., Tan, X.F., Jiang, L.H., Liu, N., Wen, J., & Liu, X.H. (2018). Performance of magnetic graphene oxide/diethylenetriaminepentaacetic acid nanocomposite for the tetracycline and ciprofloxacin adsorption in single and binary systems. *Journal of Colloid and Interface Science*, *521*, 150–159.

Li, Y., Wang, S., Zhang, Y., Han, R., & Wei, W. (2017). Enhanced tetracycline adsorption onto hydroxyapatite by Fe(III) incorporation. *Journal of Molecular Liquids*, *247*, 171–181.

Li, Z., Schulz, L., Ackley, C., & Fenske, N. (2010). Adsorption of tetracycline on kaolinite with pH-dependent surface charges. *Journal of Colloid and Interface Science*, *351*, 254–260.

Liu, M., Hou, L.A., Yu, S., Xi, B., Zhao, Y., & Xia, X. (2013). MCM-41 impregnated with a zeolite precursor: synthesis, characterization and tetracycline antibiotics removal from aqueous solution. *Chemical Engineering Journal*, *223*, 678–687.

Liu, M., Guo, B., Zou, Q., Du, M., Jia, D. (2008). Interactions between halloysite nanotubes and 2,5-bis(2-benzoxazolyl) thiophene and their effects on reinforcement of polypropylene/halloysite nanocomposites. *Nanotechnology*, 19, 205709.

Liu, N., Wang, M.X., Liu, M., Liu, F., Weng, L., Koopal, L.K., & Tan, W.F. (2012). Sorption of tetracycline on organo-montmorillonites. *Journal of Hazardous Materials*, 225–226, 28–35.

Lu, S., Tan, X., Yu, S., Ren, X., & Chen, C. (2016). Characterization of Fe(III)-saturated montmorillonite and evaluation its sorption behavior for U(VI). *Radiochimica Acta*, 104, 481–490.

Ma, Q., Wei, Y., Zhao, N., Wang, S., Zhang, B., Liu, D., & Yuan, P. (2023a). Construction of an allophane-based molecularly imprinted polymer for the efficient removal of antibiotic from aqueous solution. *Science of the Total Environment*, 903, 166464.

Ma, Q., Zhao, N., Wei, Y., Wang, S., Liu, D., & Yuan, P. (2023b). Efficient adsorption and separation of norfloxacin from water by allophane aerogel microspheres. *Separation and Purification Technology*, 327, 124808.

Macht, F., Eusterhues, K., Pronk, G.J., & Totsche, K.U. (2011). Specific surface area of clay minerals: comparison between atomic force microscopy measurements and bulk-gas (N_2) and -liquid (EGME) adsorption methods. *Applied Clay Science*, 53, 20–26.

Maged, A., Iqbal, J., Kharbish, S., Ismael, I.S., & Bhatnagar, A. (2020). Tuning tetracycline removal from aqueous solution onto activated 2:1 layered clay mineral: Characterization, sorption and mechanistic studies. *Journal of Hazardous Materials*, 384, 121320.

Melnikov, D., Reshetina, M., Novikov, A., Cherednichenko, K., Stavitskaya, A., Stytsenko, V., Vinokurov, V., Huang, W., & Glotov, A. (2023). Strategies for palladium nanoparticles formation on halloysite nanotubes and their performance in acetylene semi-hydrogenation. *Applied Clay Science*, 232, 106763.

Nie, G., Pan, B., Zhang, S., & Pan, B. (2013). Surface chemistry of nanosized hydrated ferric oxide encapsulated inside porous polymer: modeling and experimental studies. *Journal of Physical Chemistry C*, 117, 6201–6209.

Nishikiori, H., Kobayashi, K., Kubota, S., Tanaka, N., & Fujii, T. (2010). Removal of detergents and fats from waste using allophane. *Applied Clay Science*, 47, 325–329.

Obradovic, B. (2020). Guidelines for general adsorption kinetics modeling. *Hemijska industrija*, 74, 65–70.

Ortiz-Ramos, U., Leyva-Ramos, R., Mendoza-Mendoza, E., & Aragón-Piña, A. (2022). Removal of tetracycline from aqueous solutions by adsorption on raw Ca-bentonite. Effect of operating conditions and adsorption mechanism. *Chemical Engineering Journal*, 432, 134428.

Parolo, M.E., Savini, M.C., Vallés, J.M., Baschini, M.T., & Avena, M.J. (2008). Tetracycline adsorption on montmorillonite: pH and ionic strength effects. *Applied Clay Science*, 40, 179–186.

Peng, Q., Liu, M., Zheng, J., Zhou, C. (2015). Adsorption of dyes in aqueous solutions by chitosan–halloysite nanotubes composite hydrogel beads. *Microporous and Mesoporous Materials*, 201, 190–201.

Pereira, R.C., Arbestain, M.C., Kelliher, F.M., Theng, B.K.G., McNally, S.R., Macias, F., & Guitian, F. (2019). Assessing the pore structure and surface area of allophane-rich and non-allophanic topsoils by supercritical drying and chemical treatment. *Geoderma*, 337, 805–811.

Pulicharla, R., Hegde, K., Brar, S.K., & Surampalli, R.Y. (2017). Tetracyclines metal complexation: significance and fate of mutual existence in the environment. *Environmental Pollution*, 221, 1–14.

Qiao, D., Li, Z., Duan, J., & He, X. (2020). Adsorption and photocatalytic degradation mechanism of magnetic graphene oxide/ZnO nanocomposites for tetracycline contaminants. *Chemical Engineering Journal*, 400, 125952.

Qiao, H., Wang, X., Liao, P., Zhang, C., & Liu, C. (2021). Enhanced sequestration of tetracycline by Mn(II) encapsulated mesoporous silica nanoparticles: synergistic sorption and mechanism. *Chemosphere*, 284, 131334.

Ramanayaka, S., Sarkar, B., Cooray, A.T., Ok, Y.S., & Vithanage, M. (2020). Halloysite nanoclay supported adsorptive removal of oxytetracycline antibiotic from aqueous media. *Journal of Hazardous Materials*, 384, 121301.

Song, Y., Yuan, P., Du, P., Deng, L., Wei, Y., Liu, D., Zhong, X., Zhou, J. (2020). A novel halloysite-CeOx nanohybrid for efficient arsenic removal. *Applied Clay Science*, 186, 105450.

Su, Q., Pan, B., Wan, S., Zhang, W., & Lv, L. (2010). Use of hydrous manganese dioxide as a potential sorbent for selective removal of lead, cadmium, and zinc ions from water. *Journal of Colloid and Interface Science*, 349, 607–612.

Tan, D., Yuan, P., Liu, D., & Du, P. (2016). Surface modifications of halloysite. In *Nanosized Tubular Clay Minerals: Halloysite and Imogolite* (ed. Yuan, P., Thill, A., and Bergaya, F.), pp. 167–201. Elsevier, Amsterdam, Netherlands.

Thommes, M., Kaneko, K., Neimark, A.V., Olivier, J.P., Rodriguez-Reinoso, F., Rouquerol, J., & Sing, K.S.W. (2015). Physisorption of gases, with special reference to the evaluation of surface area and pore size distribution (IUPAC Technical Report). *Pure and Applied Chemistry*, 87, 1051–1069.

Tombacz, E., & Szekeres, M. (2004). Colloidal behavior of aqueous montmorillonite suspensions: the specific role of pH in the presence of indifferent electrolytes. *Applied Clay Science*, 27, 75–94.

Wang, S., Du, P., Yuan, P., Liu, Y., Song, H., Zhou, J., Deng, L., & Liu, D. (2020). Structural alterations of synthetic allophane under acidic conditions: Implications for understanding the acidification of allophanic Andosols. *Geoderma*, 376, 114561.

Wang, S., Zhang, Y., Liu, D., Yuan, P., Li, M., Du, P., Zhao, J., Yu, W., & Wang, H. (2024). Adsorption behaviors and atomistic mechanisms of iodate and iodide on hollow spherical allophane nanoparticles. *Applied Clay Science*, 250, 107293.

Wang, W., Gao, M., Cao, M., Dan, J., & Yang, H. (2021). Self-propagating synthesis of Zn-loaded biochar for tetracycline elimination. *Science of the Total Environment*, 759, 143542.

Wang, W.B., Lu, T.T., Chen, Y.L., Tian, G.Y., Sharma, V.K., Zhu, Y.F., Zong, L., & Wang, A.Q. (2019). Mesoporous silicate/carbon composites derived from dye-loaded palygorskite clay waste for efficient removal of organic contaminants. *Science of the Total Environment*, 696, 133955.

Wu, M., Zhao, S., Jing, R., Shao, Y., Liu, X., Lv, F., Hu, X., Zhang, Q., Meng, Z., & Liu, A. (2019). Competitive adsorption of antibiotic tetracycline and ciprofloxacin on montmorillonite. *Applied Clay Science*, 180, 105175.

Xiao, B., Wu, M., Wang, Y., Chen, R., & Liu, H. (2021). Sulfite activation and tetracycline removal by rectangular copper oxide nanosheets with dominantly exposed (001) reactive facets: performance, degradation pathway and mechanism. *Chemical Engineering Journal*, 406, 126693.

Xiong, W., Zeng, G., Yang, Z., Zhou, Y., Zhang, C., Cheng, M., Liu, Y., Hu, L., Wan, J., Zhou, C., Xu, R., & Li, X. (2018). Adsorption of tetracycline antibiotics from aqueous solutions on nanocomposite multi-walled carbon nanotube functionalized MIL-53(Fe) as new adsorbent. *Science of the Total Environment*, 627, 235–244.

Xu, L., Zhang, H., Xiong, P., Zhu, Q., Liao, C., & Jiang, G. (2021). Occurrence, fate, and risk assessment of typical tetracycline antibiotics in the aquatic environment: a review. *Science of the Total Environment*, 753, 141975.

Yan, L., Liu, Y., Zhang, Y., Liu, S., Wang, C., Chen, W., Liu, C., Chen, Z., & Zhang, Y. (2020). ZnCl2 modified biochar derived from aerobic granular sludge for developed microporosity and enhanced adsorption to tetracycline. *Bioresource Technology*, 297, 122381.

Yang, Q., Hong, H., & Luo, Y. (2020). Heterogeneous nucleation and synthesis of carbon dots hybrid Zr-based MOFs for simultaneous recognition and effective removal of tetracycline. *Chemical Engineering Journal*, 392, 123680.

Yang, X., Cai, J., Chen, L., Cao, X., Liu, H., Liu, M. (2021). Green detergent made of halloysite nanotubes. *Chemical Engineering Journal*, 425, 130623.

Yang, Y., Hu, X., Zhao, Y., Cui, L., Huang, Z., Long, J., Xu, J., Deng, J., Wu, C., & Liao, W. (2017). Decontamination of tetracycline by thiourea-dioxide-reduced magnetic graphene oxide: effects of pH, ionic strength, and humic acid concentration. *Journal of Colloid and Interface Science*, 495, 68–77.

Yu, W.B., Xu, H.F., Tan, D.Y., Fang, Y.H., Roden, E.E., & Wan, Q. (2020). Adsorption of iodate on nanosized tubular halloysite. *Applied Clay Science*, 184, 105407.

Yuan, P., Southon, P.D., Liu, Z., Green, M.E.R., Hook, J.M., Antill, S.J., & Kepert, C.J. (2008). Functionalization of halloysite clay nanotubes by grafting with γ-aminopropyltriethoxysilane. *Journal of Physical Chemistry C*, 112, 15742–15751.

Yuan, P., Tan, D., & Annabi-Bergaya, F. (2015). Properties and applications of halloysite nanotubes: recent research advances and future prospects. *Applied Clay Science*, 112, 75–93.

Yucelen, G.I., Choudhury, R.P., Leisen, J., Nair, S., & Beckham, H.W. (2012). Defect structures in aluminosilicate single-walled nanotubes: a solid-state nuclear magnetic resonance investigation. *Journal of Physical Chemistry C*, *116*, 17149–17157.

Zhang, S., Li, Y., Shi, C., Guo, F., He, C., Cao, Z., Hu, J., Cui, C., & Liu, H. (2018). Induced-fit adsorption of diol-based porous organic polymers for tetracycline removal. *Chemosphere*, *212*, 937–945.

Zhang, W., Wang, L., Su, Y., Liu, Z., & Du, C. (2021). Indium oxide/halloysite composite as highly efficient adsorbent for tetracycline removal: key roles of hydroxyl groups and interfacial interaction. *Applied Surface Science, 566*, 150708.

Zhang, Z., Lan, H., Liu, H., & Qu, J. (2015). Removal of tetracycline antibiotics from aqueous solution by amino-Fe (III) functionalized SBA15. *Colloids and Surfaces A: Physicochemical and Engineering Aspects*, *471*, 133–138.

Zhu, L., Zhu, R., Xu, L., & Ruan X. (2007). Influence of clay charge densities and surfactant loading amount on the microstructure of CTMA–montmorillonite hybrids. *Colloids and Surfaces A: Physicochemical and Engineering Aspects*, *304*, 41–48.